Arabian Journal of Chemistry (2021) **14**, 102992

King Saud University

Arabian Journal of Chemistry

www.ksu.edu.sa
www.sciencedirect.com

ORIGINAL ARTICLE

Fabrication of exchange coupled hard/soft magnetic nanocomposites: Correlation between composition, magnetic, optical and microwave properties

Y. Slimani [a,*], N.A. Algarou [a,b], M.A. Almessiere [a,*], A. Sadaqat [c], M.G. Vakhitov [d,e], D.S. Klygach [d,e], D.I. Tishkevich [d,f], A.V. Trukhanov [d,f,g,*], S. Güner [h], A.S. Hakeem [i], I.A. Auwal [j], A. Baykal [k], A. Manikandan [l], I. Ercan [a]

[a] *Department of Biophysics, Institute for Research and Medical Consultations (IRMC), Imam Abdulrahman Bin Faisal University, P.O. Box 1982, Dammam 31441, Saudi Arabia*
[b] *Department of Physics, College of Science, Imam Abdulrahman Bin Faisal University, Dammam 31441, Saudi Arabia*
[c] *Department of Mechanical and Energy Engineering, College of Engineering, Imam Abdulrahman Bin Faisal University, Dammam 31441, Saudi Arabia*
[d] *South Ural State University, 454080 Chelyabinsk, Russia*
[e] *Ural Federal University, 620002 Ekaterinburg, Russia*
[f] *SSPA "Scientific-Practical Materials Research Centre of NAS of Belarus", Minsk 220072, Belarus*
[g] *National University of Science and Technology MISiS, 119049 Moscow, Russia*
[h] *Institute of Inorganic Chemistry, RWTH Aachen University, Aachen 52074, Germany*
[i] *Center of Research Excellence in Nanotechnology (CENT), King Fahd University of Petroleum and Minerals (KFUPM), Dhahran, Saudi Arabia*
[j] *Department of Chemistry, Sule Lamido University, Kafin Hausa 731, Nigeria*
[k] *Department of Nanomedicine Research, Institute for Research and Medical Consultations (IRMC), Imam Abdulrahman Bin Faisal University, P.O. Box 1982, 31441 Dammam, Saudi Arabia*
[l] *Department of Chemistry, Bharat Institute of Higher Education and Research (BIHER), Bharath University, Chennai 600073, Tamil Nadu, India*

Received 28 November 2020; revised 3 January 2021; accepted 4 January 2021

* Corresponding authors at: Institute for Research and Medical Consultations (IRMC), Imam Abdulrahman Bin Faisal University, P.O. Box 1982, 31441 Dammam, Saudi Arabia (Y. Slimani & M.A. Almessiere). South Ural State University, 454080 Chelyabinsk, Russia (A.V. Trukhanov).
E-mail addresses: yaslimani@iau.edu.sa, slimaniyassine18@gmail.com (Y. Slimani), malmessiere@iau.edu.sa (M.A. Almessiere), truhanov86@-mail.ru (A.V. Trukhanov).
Peer review under responsibility of King Saud University.

Production and hosting by Elsevier

https://doi.org/10.1016/j.arabjc.2021.102992

Available online 10 January 2021

KEYWORDS

Hard/soft magnetic nanocomposites;
Optical-structural features;
Magnetic-structural features;
Exchange coupling;
Microwave features

Abstract This paper studied the exchange coupling performance beside structural and microwave properties of $SrFe_{12}O_{19}$ (SFO) and x($CoTm_{0.01}Tb_{0.01}Fe_{1.98}O_4$) (CoTmTb) ($x \leq 3.0$) hard/soft ferrites nanocomposites (NCs). The structure and morphology of NCs were investigated by XRD, SEM, TEM and HR-TEM. Diffuse reflectance spectroscopic (DRS) measurements were applied on hexagonal ferrite, on spinel ferrite nanoparticles and on hard/soft NCs to specify the optical properties. Estimated E_g data are in a range between 1.32 and 1.79 eV. The magnetic properties were also inspected via measurements of magnetization (M) against magnetic field (H) at 300 K (RT) and 10 K (LT). The measurements performed at RT along with the plots of dM/dH versus H indicated that the NCs display good magnetic properties (exchange coupling behavior). The magnetic parameters such as (M_s, M_r, and H_c) show an enhancement in their values with an increasing the soft content at RT. Similarly, the maximum energy product $(BH)_{max}$ rises and reaches its max value for SFO/3(CoTmTb) NCs. Microwave properties of the SFO/x(CoTmTb) NCs were measured in the frequency range 33–50 GHz. From measured S11 and S21 parameters the main electrodynamic characteristics – permittivity and permeability (real and imaginary parts) were computed.

1. Introduction

The research area of hard M-type and soft spinel ferrites have been well established over the past decades (Vinnik et al., 2020; Singh et al., 2018; Mameli et al. 2019; Thakur et al. 2020). Indeed, these nanocrystalline ceramic magnets have demonstrated anattractive electromagnetic properties that can potentially address the challenges of today's electronic devices (Wang et al., 2015; Khandani et al., 2019). For instance, the issue of the electromagnetic interference (EMI) resulting from the excessive use of high-frequency electronic devices, can be controlled by microwave absorbing barium or strontium ($BaFe_{12}O_{19}$/$SrFe_{12}O_{19}$ or BFO/SFO) hexaferrite owing to their dielectric magnetic lose properties (Zhang et al., 2012; Kumar et al., 2013; Trukhanov et al., 2017; González-Angeles et al., 2004). Materials for effective electromagnetic absorption must have several features: high values of imaginary parts of the magnetic permeability and electrical permittivity; broad bandwidth of the electromagnetic absorption (Harris, 2011; Tong et al., 2016). Recently soft/hard ferrite composites attract great attention due to their values for microwave absorption, magnetization and coercivity properties (Meng et al., 2019; Han et al., 2018). Good magnetic characteristics of the composite can be result of the exchange coupling between hard/soft phases. There are a lot of papers that explained the features of the magnetic properties in hard/soft composites, such as $Ni_{0.5}Zn_{0.5}Fe_2O_4$/BFO (Meng et al., 2019), BFO/$CoFe_2O_4$ (Yang et al., 2015), $NiFe_2O_4$/$SrCo_{0.2}Fe_{11.8}O_{19}$ (Xia et al., 2018a), $(Ba_{0.5}Sr_{0.5}Fe_{12}O_{19})_{1-x}(CoFe_2O_4)_x$ (Harikrishnan et al., 2016), $Mn_{0.6}Zn_{0.4}Fe_2O_4$/$Sr_{0.85}Ba_{0.15}Fe_{12}O_{19}$ (Xia et al., 2018b), $Ni_{0.5}Zn_{0.5}Fe_2O_4$/SFO (Han et al., 2018), SFO/$Ni_{0.5}$-$Zn_{0.5}Fe_2O_4$ (Song et al., 2011), SFO/$Ni_{0.7}Zn_{0.3}Fe_2O_4$ (Radmanesh and Seyyed Ebrahimi, 2012). Nowadays, composites based on soft/hard magnetic materials attract great interest due to improve the magnetic characteristics. It was observed strong correlation between phase ratio, chemical composition of each phase, microstructure, magnetic and microwave properties.

Although substitution using several, di-, tri- and tetravalent cations (Mg^{2+} Zn^{2+}, Tb^{3+}, Ga^{3+}, Li^{3+}-Pr^{3+}, Y^{3+}, Sn^{4+} and Zr^{4+}) have been investigated in an attempt to simultaneously augment the saturation magnetization (M_s) and coercivity (H_c) of the M-type hexaferrite (Trukhanov et al., 2017; González-Angeles et al., 2004; Almessiere et al., 2019a; Ghimire et al., 2020; Baykal et al., 2017). However, most of the reported single-phase magnetic materials could not sufficiently satisfy the requirement of an ideal microwave absorbing materials, namely: a wider range of working frequency, large absorption peak, and ability to form a thin absorption layer (Hazra et al., 2015). Thus, syntheses of the composite material become a promising approach to enhance magnetic, electric, and microwave properties of the ceramic magnets. This could be achieved by combining hard and soft ferrite into a dual-phase magnetic NCs, commonly called the exchange-spring magnets. Consistent with this concept, pioneers by Hawking and Kneller in 1991 (Kneller and Hawig, 1991) exchange-spring (also called the exchanged coupled-composites) magnets might poses the high values of H_c and M_s resulting from parent phases of hard and soft ferrite respectively. This occurs when both magnetic species appropriately dispersed to form a mutually exchanged couple phases (Pahwa et al., 2020). The exchange-couple magnets, thus, have a wide compositional flexibility. The product shows gentle demagnetization with a regular rotation of spin, in contrast to a steeper hysteresis curve displayed by the non-couple phase owing to differences in the switching of hard and soft spin (Xiong et al., 2016).

A significant number of studies of exchange-coupling NC ferrites for use in microwave applications have been reported (Pahwa et al., 2020; Mehdipour and Shokrollahi, 2013; Hilczer et al., 2016). It is well understood that partial substitution of cation(s) into a pristine ferrite lattice would an augment it's magnetic, electrical, and microwave properties (Trukhanov

et al., 2018; Wang et al., 2019), therefore, a more promising exchange-spring could be produced when cation substituted hard and soft ferrites precursors are used. Further, the Tb^{3+}-substituted cobalt ferrite nanoparticles was exhibited a direct effect on energy band gap (Eg) values and found that is increased with incresing the ratio of Tb^{3+}. Magnetization versus magnetic field was demonstrated that the Tb^{3+} substitutions strongly influenced the magnetization data (Sadaqat et al., 2019). Likewise, the Tm substituted cobalt ferrite nanoparticles showed a fluctuating in band gap energy (Eg) with raising the amount of Tm^{3+}. An remarkable effects of Tm^{3+} substitution on magnetizations data such as Ms, Mr, and n_B with increasing the Tm^{3+} concentration (Almessiere et al., 2019d). Additionally, we are passionate about Terbium (Tb^{+}) and Thulium (Tm^{3+}) ions substitutions, where 0.01 M substitution in pristine $SrFe_{12}O_{19}$ increased the M_s, remanence (M_r) and magnetic moment (n_B) of the solid (Almessiere et al., 2019b). Similarly, Tm-Tb co-substituted Co-Ni nano-spinel ferrites presented a divergence in magnetic parameters are which defined on base of redistribution of cations, variations crystallites and/or grains size, canting effects, surface spins effects, super-exchange interaction strength (Almessiere et al., 2020f). Besides, several reports have shown improvement in the magnetic properties, particularly in exchange-coupling behavior by using co-substituted in hexaferrite or spinel ferrite side in hard/soft nano-compositions. Newly, we investigated the exchange-coupling effects in a series of $SrTb_{0.01}Tm_{0.01}Fe_{11.98}O_{19}/CoFe_2O_4$ hard/soft nanocomposites and their morphological, structural and magnetic properties. We found that amongst the various prepared composites, the exchange coupling among the soft and hard ferrite grains was existed and a radical rise in saturation magnetization (Ms), remanence (Mr) and coercivity (Hc) was observed on increasing the content of the soft phase (x) (N. A. Algarou, et al., 2020a).

Accordingly, we study a magnetic and exchanged-spring composite structure by substituted Tb/Tm in cobalt ferrite: SFO/x(CoTmTb). A one-pot sol-gel auto combustion route was employed. Unlike the physical mixing method (Torkian et al., 2016), sol-gel auto combustion is simple and economical, and most importantly, it provides the nanocrystals with a narrow size distribution. The ionic redox reaction is involved which results in an exothermic process that produces high thermal energy due to combustion and consequently, a stronger chemical bonding between the chemical species is established, thus, the desired magnetic phase is crystallized within a short time (Yue et al., 2004).

2. Experimental procedure

The SFO and CoTmTb were synthesized separately with sol–gel auto-combustion method. For the synthesis of hard-soft NCs, initially a stoichiometric amount of $Sr(NO_3)_2$, $Fe(NO_3)_3 \cdot 9H_2O$ and $C_6H_8O_7$ were thawed in 60 ml deionized water with continuing stirrer at 85 °C for 40 min to produce the SFO solution. For preparing CoTmTb, the $Co(NO_3)_2 \cdot 6H_2O$, Tm_2O_3, Tb_4O_7, and $Fe(NO_3)_3 \cdot 9H_2O$ were used. The stoichiometric amounts of the Tm_2O_3 and Tb_4O_7 were first thawed in 10 ml acid solution containing HCl and HNO_3 at 180 – 200 °C with stirring until get clear solutions. The oxides solutions were mingled with metal nitrates in 60 ml of distilled water. Subsequently the pH of SFO and CoTmTb solutions were controlled by ammonium solution to regulated at 7 and at that point the temp was raise up at 160 °C for 50 min then at 380 °C to get black ash. The final powder was calcinated at 1000 °C for SFO and 950 °C for CoTmTb for a period around 6 h. In order to prepare hard/soft SFO/x(CoTmTb) ($x \leq 3.0$) NCs with both SFO and CoTmTb solutions were mixed together following *one-pot* citrate combustion approach. The pH value of the mixture was attuned at 7 by ammonium solution at 180 °C for 50 min then raised up to 370 °C to get black powder. The final compositions were annealed at 950 °C for 6 h (Kubelka, 1948; Kubelka and Munk, 1931).

The structure of hard/soft NCs was analyzed through XRD diffractometer from Rigaku D/MAX-2400 (Cu Kα radiation). The morphology was obtained through FE-SEM (Lyra3, Tescan, Brno, Czech Republic) connected (EDX) energy-dispersive X-ray and Transmission electron microscope (TEM) (FEI Titan ST Microscopes). The optical properties were carried out through UV–visible diffuse reflectance (DR) spectrophotometer from JASCO over a range of 200–800 nm. The magnetic measurements of samples were executed by Quantum Design PPMS DynaCool-9 coupled linked with a head of vibrating sample magnetometer (VSM). Microwave properties were obtained by using vector network analyzer (R&S model ZVA50) in 33–50 GHz range.

3. Results and discussion

3.1. Structure

Fig. 1 represents the XRD patterns of SFO, CoTmTb and hard/-soft SFO/x(CoTmTb) ($x \leq 3.0$) NCs. Fig. 1a showed that the typical peaks are matched with the M-type hexaferrite and spinel ferrite, individually. It is noted from XRD pattern of the CoTmTb that there is a minor secondary phase of the $TbFeO_3$ and Fe_2O_3 due to the solubility limit of a rare earth ions as a consequence of larger ionic radii. The structure of hard/soft SFO/x (CoTmTb) NCs with diverse weight percentages were demonstrated in Fig. 1b. The XRD diffraction pattern of nanocompositions were exhibited an efficaciously construction of the hard/soft encompassing M-type hexaferrite with a cubic spinel ferrite with no formation of any undesirable phases, an evidence of the efficiency of the preparation method. Furthermore, the pattern displayed a variation in intensity due to an increase the spinel ferrite amount. The structure parameters of the hard/soft SFO/x(CoTmTb) ($x \leq 3.0$) NCs and the percentage of each hard and soft ferrites were evaluated by Match 3! FullProf software as presented in Table 1.

It is clear that the structural parameters of the hard ferrite were fluctuating when increased the ratio of spinel part due to the change in solubility among hard and soft phases (Torkian et al., 2016). The average crystal size of the SFO and CoTmTb were obtained by implementing Scherrer's equation on the typical peaks of SFO and CoTmTb ferrites. It is noteworthy, that the average crystal size of each SFO and CoTmTb ferrites are grew slightly when increased through fraction of spinel ferrite. Also, it was found that the average crystal size of the SFO is about 53% larger than the CoTmTb as clear from Table 1 (Torkian et al., 2016). The alteration in crystal size growth of both phases is due to boundary movement of grans which lead to suppresses growth of the spinel phase (Mousavi Ghahfarokhi et al., 2020).

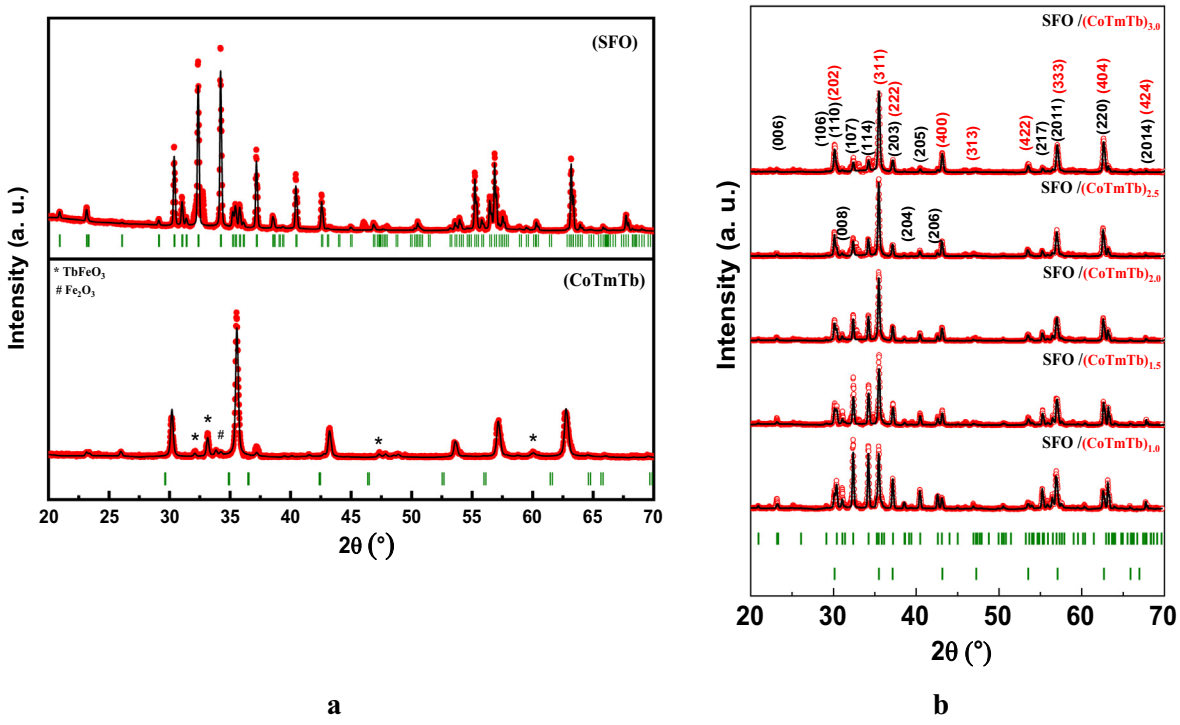

Fig. 1 XRD powder patterns of (a) SFO and CoTmTb separately, (b) hard/soft SFO/x(CoTmTb) ($x \leq 3.0$) NCs.

Table 1 The structure parameters were calculated for SFO/x(CoTmTb) ($x \leq 3.0$) NCs.

Product	D_{XRD} (nm)		Hard phase			Soft phase	
	Soft	Hard	a = b (Å)	c (Å)	Fraction (%)	a = b = c (Å)	Fraction (%)
SFO	–	40.7 ± 0.4	5.8816	23.0485	100	–	–
SFO/1.0(CoTmTb)	24.8 ± 0.2	60.5 ± 0.2	5.8823	23.0231	72 ± 0.5	8.3960	28 ± 0.5
SFO/1.5(CoTmTb)	34.0 ± 0.3	69.7 ± 0.3	5.8774	23.0040	57.5 ± 0.3	8.3897	42.4 ± 0.3
SFO/2.0(CoTmTb)	38.0 ± 0.2	72.1 ± 0.2	5.8812	23.0178	54.9 ± 0.4	8.3890	45.1 ± 0.4
SFO/2.5(CoTmTb)	38.2 ± 0.2	73.1 ± 0.2	5.8823	23.0141	32.7 ± 0.7	8.3884	67.3 ± 0.7
SFO/3.0(CoTmTb)	42.5 ± 0.3	81.5 ± 0.3	5.8806	23.0009	29.3 ± 0.4	8.3875	70.7 ± 0.4
CoTmTb	48.6 ± 0.5	–	–	–	–	8.3665	100

3.2. Microstructural analysis of hard/soft nanocomposites

Fig. 2 shows the SEM images of hard/soft SFO/x(CoTmTb) ($x \leq 3.0$) NCs. The images revealed the two different morphologies: cubic and hexagonal plate-lets particles that belonged to spinel and M-type hexaferrites, respectively. The compositions morphology showed vividly a big hexagonal particle cover up by a cluster of agglomerated cubic particles due to the magnetic dipole amongst the magnetic nanoparticles. It is clear that the amount of cubic particles increased with the increasing of the spinel ferrite fractions until the whole hexagonal plate-lets particles covered completely by accumulating cubic particles. The EDX spectra of the hard/soft SFO/x (CoTmTb) (x = 1.5 and 3) NCs are presented in Fig. 3. The EDX spectra exhibited the consisted elements and there weight percentage of the hard/soft NCs. Additionally, the morphology and structure of the hard/soft SFO/x(CoTmTb) (x = 1 and 2) NCs were approved by TEM and HR-TEM as disclosed from Fig. 4. The TEM presented the integration phase between M-type hexaferrite and spinel ferrite. The HR-TEM image was introduced the interplanar which consistent with the hard and soft phases.

3.3. Optical properties

The optical properties were explored on pristine SFO nanoparticles (NPs), Tm^{3+} and Tb^{3+} ions substituted cobalt spinel ferrite and hard/soft SFO/x(CoTmTb) ($x \leq 3.0$) NCs with various spinel contents using diffuse reflectance (DR %) UV–vis spectrophotometer. DR % spectra were recorded in (200–800) nm wavelength (λ) region and are presented in Fig. 5.

Only one spectrum which belongs to the SFO NPs exhibits remarkably distinct behavior. Reflectance intensity of this spectrum stays almost the same with a ~17.50% magnitude between 200 nm and 600 nm and then above 600 nm abruptly increases to maximum 53.40% corresponding to 800 nm wavelength. The intensities of all other spectra are in a narrow band

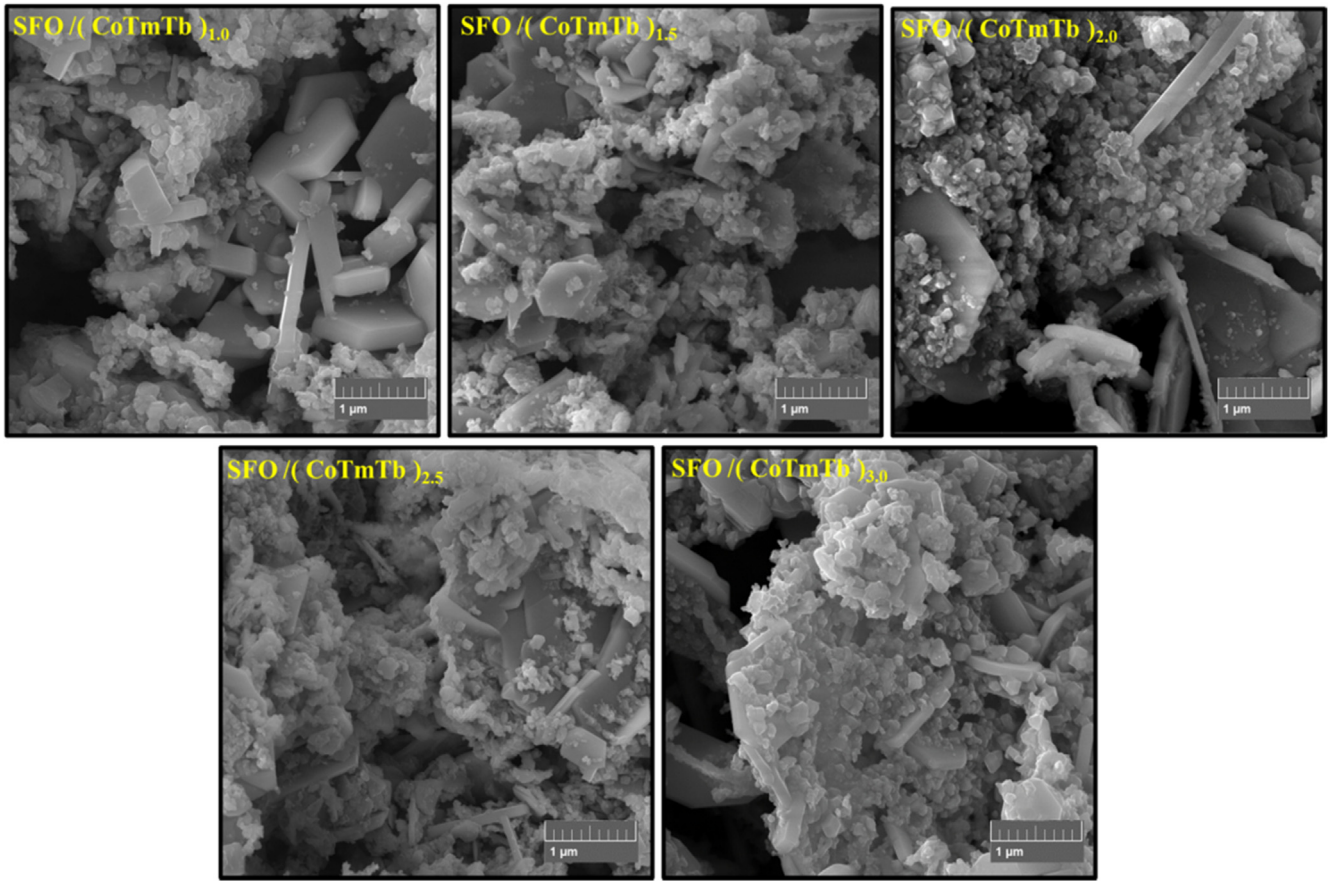

Fig. 2 SEM images of hard/soft SFO/x(CoTmTb) ($x \leq 3.0$) NCs.

of (13.75–24.45) % for the whole sweep region of incident radiation.

Optical excitation of electrons provokes an increment of the absorbance in the wavelength region that is compatible with the activation energy of the electrons, which enables us to define the position of absorption edge.

When the goal is to determine the energy band gap (E_g), one generally applies to the Kubelka–Munk (K-M) theory to be able to utilize from the reflectance spectra of semiconducting powder samples (Tauc et al., 1966; Auwal et al., 2016a). In this theory, the behavior of the light beam through a dispersing powder medium is described as a function of the scattering (S) and absorption (K) coefficients. Hence, an absolute diffuse reflectance (R_∞) dependent Kubelka–Munk function, $F(R_\infty)$ for any λ is described as a division of those coefficients and corresponds to the absorbance (α)

$$F(R_\infty) = \frac{K}{S} = \frac{(1-R_\infty)^2}{2R_\infty} \equiv \alpha \tag{1}$$

where the ∞ defines an infinitely thick layer formed by a nanocrystalline powder in the sample holder of device. For the semiconducting powder samples that have disordered electronic structure, the DR % spectra are characterized by the presence of nearby states of the valence and conduction bands, and E_g is generally estimated via the well-known Tauc expression (Auwal et al., 2016b; Auwal et al., 2016c):

$$(\alpha h\upsilon)^n = (F(R_\infty)h\upsilon)^n = A(h\upsilon - E_g) \tag{2}$$

where $A$is the dimensionless proportionality constant, $h\upsilon$ is the energy of incident photon in unit of eV, power n = 2 determines the type of electronic transition as a direct allowed transition. The magnitude of band gaps is estimated from the extrapolation of the linear least squares fit of $(F(R_\infty)h\upsilon)^2$ to zero, by plotting $(F(R_\infty)h\upsilon)^2$ versus photon energy ($h\upsilon$) graphs. Fig. 6 indicates the Tauc plots belonging to our all type of powder samples with linear fitting lines and the estimated band gap magnitudes.

Sr hexaferrite NPs have maximum E_g value as equal to 1.83 eV. The CoTmTb spinel ferrite sample has 1.36 eV band gap. The hard/soft SFO/x(CoTmTb) ($x \leq 3.0$) NCs have band gap values in an interval between 1.32 and 1.47 eV. There is a tendency particularly for the x = 1.0, 1.5, 2.0 contents that soft phase reduces the E_g of composite. However, for the contents of x = 2.5 and 3.0, it is observed a significant increase at E_g from 1.33 eV to 1.47 eV and 1.45 eV, respectively. XRD results in Table 1 provides that particle sizes are between 30 nm and 81.5 nm. There is almost an ongoing growth on size of each hard and soft particles with increasing content of soft phase, too. Both minimum 30 nm particle size and ongoing growth do not provide us a possibility to interpret the quantum confinement effect as a reason of increase at E_g. Burstein-Moss effect is another reason to increasing band gap magnitudes in the case of increasing free carrier concentration in the material. But, we do not have any data to assign increasing free electron concentration as a reason of E_g widening. Hence, further investigations are needed.

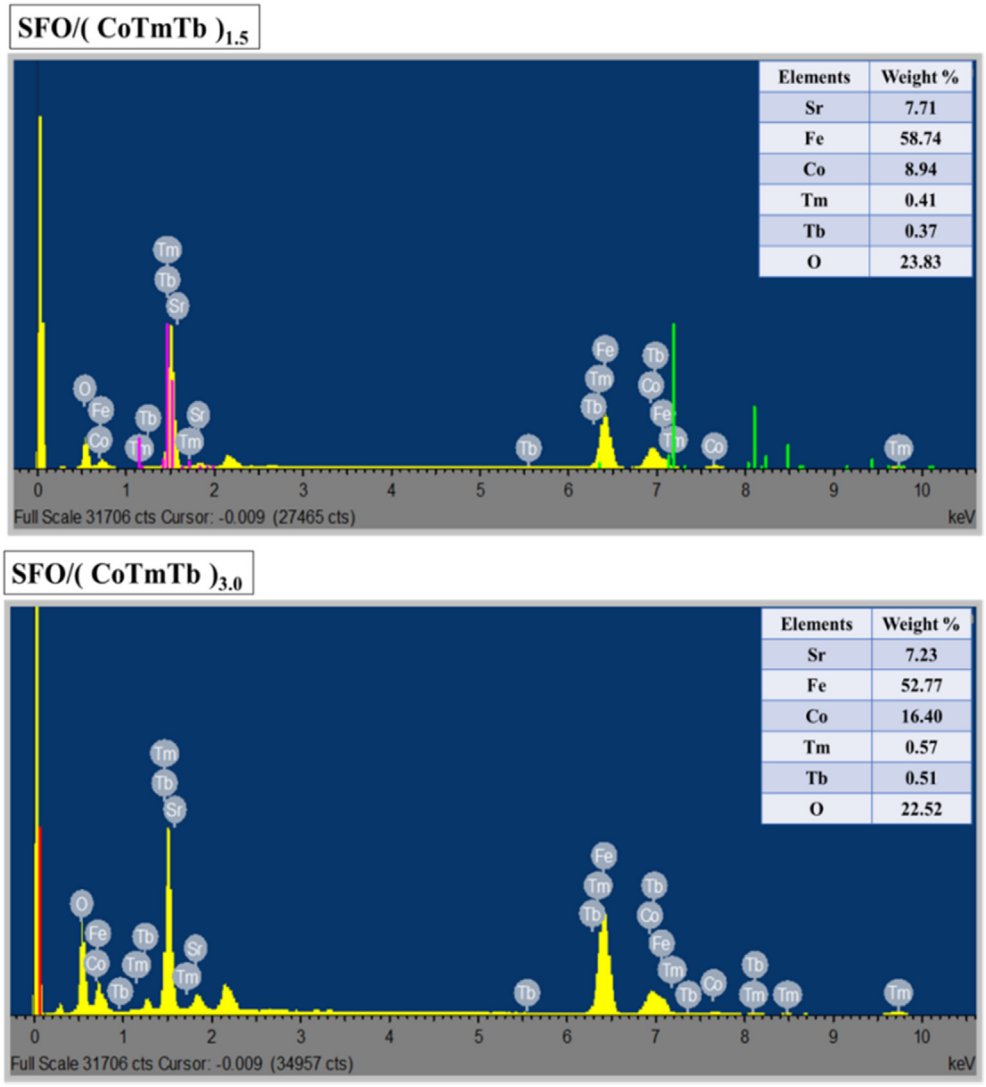

Fig. 3 EDX spectra of hard/soft SFO/x(CoTmTb) (x = 1.5 and 2.0) NCs.

All powder samples synthesized via sol–gel method have E_g values in the order of semiconducting materials. Our group and other research groups reported many band gaps for pristine SFO NPs having magnitudes between 1.74 and 2.10 eV in the literature (Auwal et al., 2017; Güner et al., 2020; Auwal et al., 2016d; Doma et al., 2012; Javidan et al., 2014; Almessiere et al., 2019c; Sadaqat et al., 2019). Similarly, the reported data are in a wider range between 1.11 and 2.70 eV for pristine $CoFe_2O_4$ (Gharibshahi et al., 2020; Josh et al., 2019; Algarou et al., 2020a; Algarou et al., 2020b). However, there are not any reported E_g data belonging to hard/soft SFO/x(CoTmTb) NCs.

3.4. Magnetic properties

The magnetic measurements of pure SFO hexaferrite and pure CoTmTb spinel ferrite samples were conducted by using the VSM technique at RT and T = 10 K, under the application of an external magnetic field up to $H = \pm 10$ kOe. *M-H* magnetization hysteresis loops of $SrFe_{12}O_{19}$ sample at both measured temperatures (RT = 300 K and LT = 10 K) exhibits ferrimagnetic behavior (Fig. 7). The different prepared samples (as well the nanocomposites discussed after) are not saturated at an applied magnetic field of 10 kOe. Accordingly, the law of approaching to saturation (LAS) at high fields was used to estimate the values of saturation magnetization (M_s) via plotting the magnetization (M) versus $1/H^2$ (since $M = M_s\left(1 - \frac{b}{H^2}\right)$). M_s value will be extracted from intercept. M_s value increases with decreasing the temperature from 300 down to 10 K. The magnetic saturation (M_s) and remanent magnetization (M_r) are about 46.2 and 27.7 emu/g at RT and 67.3 and 39.2 emu/g at LT. Whereas, the coercivity decreases with decreasing the temperature, which is a characteristic feature of the M-type hexagonal ferrites. The coercivity values are equal to H_c = 4.14 kOe at 300 K and H_c = 2.56 kOe at 10 K. According to the Stoner-Wohlfarth (S-W) theory, the coercive field (H_c) strongly depends on the magnetic field that is required to overcome magnetic anisotropy barrier (Topkaya, 2017). With decreasing (or increasing) of the effective magnetic anisotropy, an external magnetic field needed for

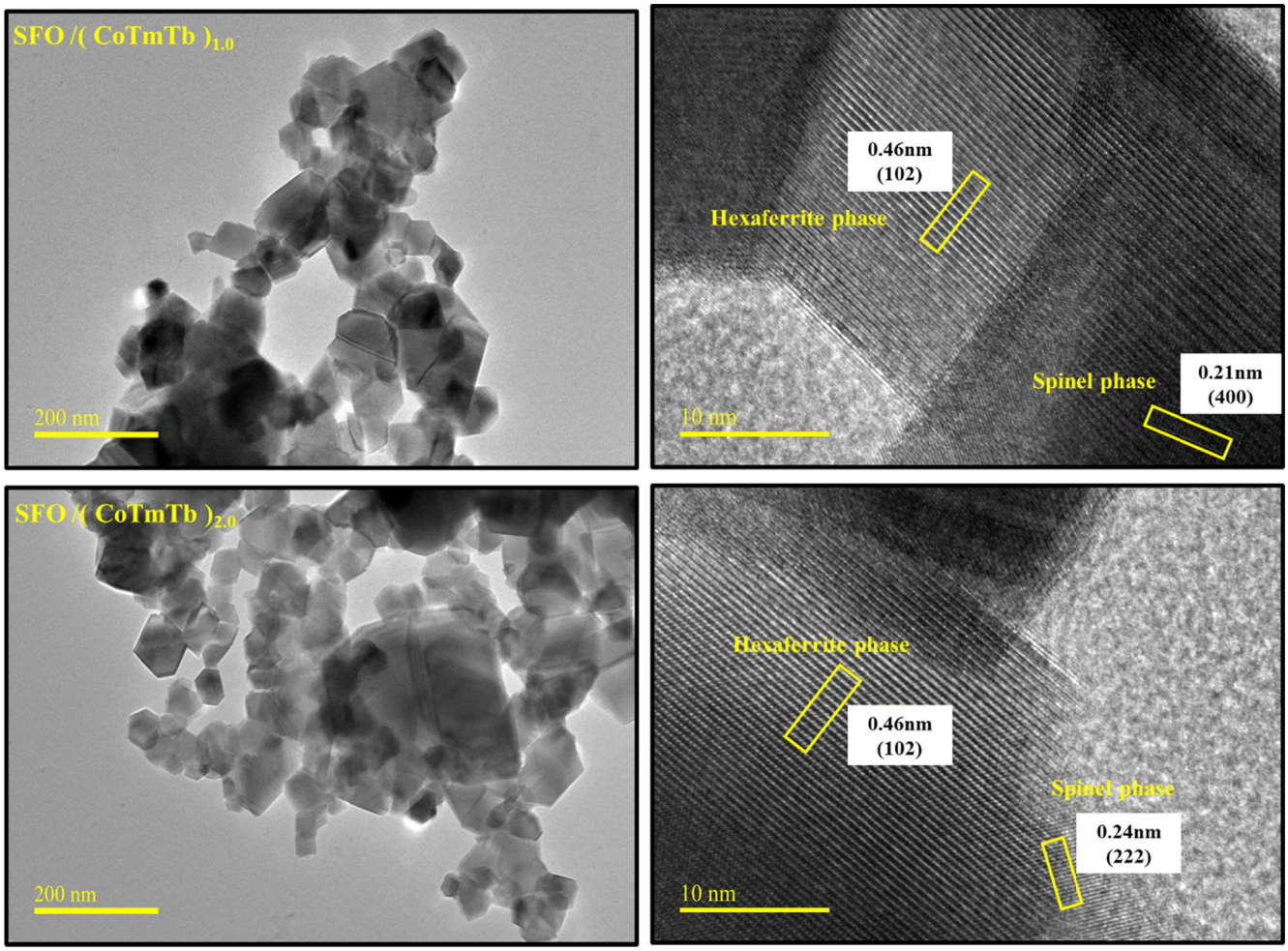

Fig. 4 TEM and HR-TEM images of hard/soft SFO/x(CoTmTb) (x = 1.0 and 2.0) NCs.

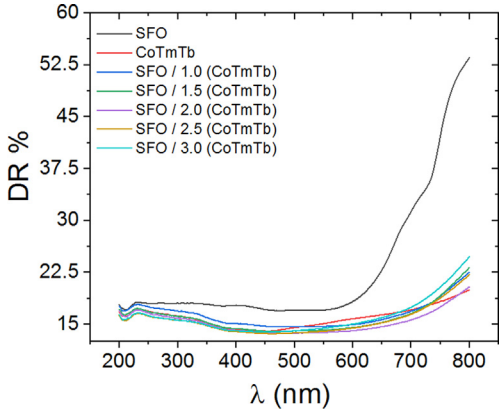

Fig. 5 DR % spectra of the $SrFe_{12}O_{19}$ hexaferrite, $CoTm_{0.01}Tb_{0.01}Fe_{1.98}O_4$ spinel ferrite and hard/soft SFO/x(CoTmTb) ($x \leq 3.0$) NCs.

spin reversal decreases (or increases), too. This is one of the plausible reasons for the variation in coercive fields. The other plausible factor altering the coercivity is the saturation magnetization (M_s). Indeed, the coercivity is mainly correlated with change in the saturation magnetization values. According to the S-W theory, H_c increases when the effective magnetic anisotropy increases. Nevertheless, if M_s increases, H_c value will decrease. In the present study, due to the reduction in thermal fluctuations at lower temperatures, the effective magnetic anisotropy increases within hexaferrite system. Furthermore, it is clear that the M_s value is increased for SFO hexaferrite with decreasing the temperature from 300 down to 10 K. Taking into consideration these observations, the coercive field (H_c) will diminish accordingly. Another plausible reason for the decreasing in H_c value with decreasing temperature could be the reduction in the anisotropy field (Shams et al., 2016).

Similarly, CoTmTb sample showed opened *M-H* hysteresis loops with large coercivity of 0.88 kOe at RT and 4.00 kOe at LT. Accordingly, this sample also displayed a ferrimagnetic behavior at both RT and LT. M_s and M_r values are equal to 65.4 and 30.8 emu/g at 300 K, and to 61.6 and 48.9 emu/g at 10 K. The reason for the high magnetization in this compound is the inclusion of rare-earth (RE) ions of Tb^{3+} and Tm^{3+} ions having the magnetic moments of about 9.5 and 7.5 μ_B, which are larger compared to those of Fe^{3+} ions (5 μ_B). The large coercivity could be due to the enhanced magnetocrystalline anisotropy. The effective magnetic anisotropy increases with decreasing temperature because the content of the Co^{2+} ions in the octahedral (B) sites increases with decreasing temperature. Taking into account that the spins of Fe^{3+} ions in tetra-

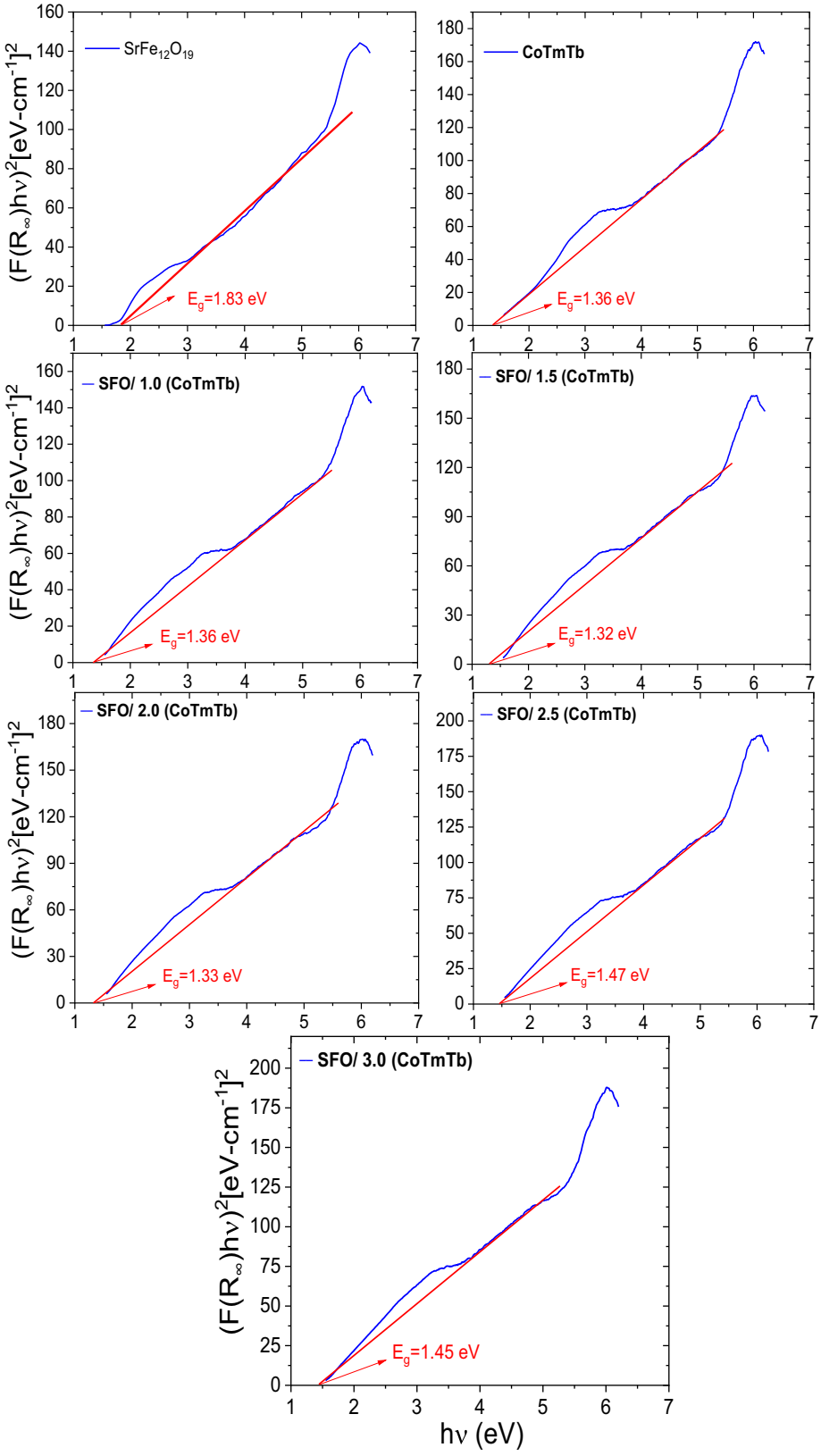

Fig. 6 Tauc plots of the SFO hexaferrite, CoTmTb spinel ferrite and hard/soft SFO/x(CoTmTb) ($x \leq 3.0$) NCs.

hedral (A) sites and Co^{2+} ions in octahedral sites are anti-parallel in their arrangement, this will lead to an increase in the ferrimagnetism. Furthermore, the reason for the increase in coercivity with decrease in temperature can be understood

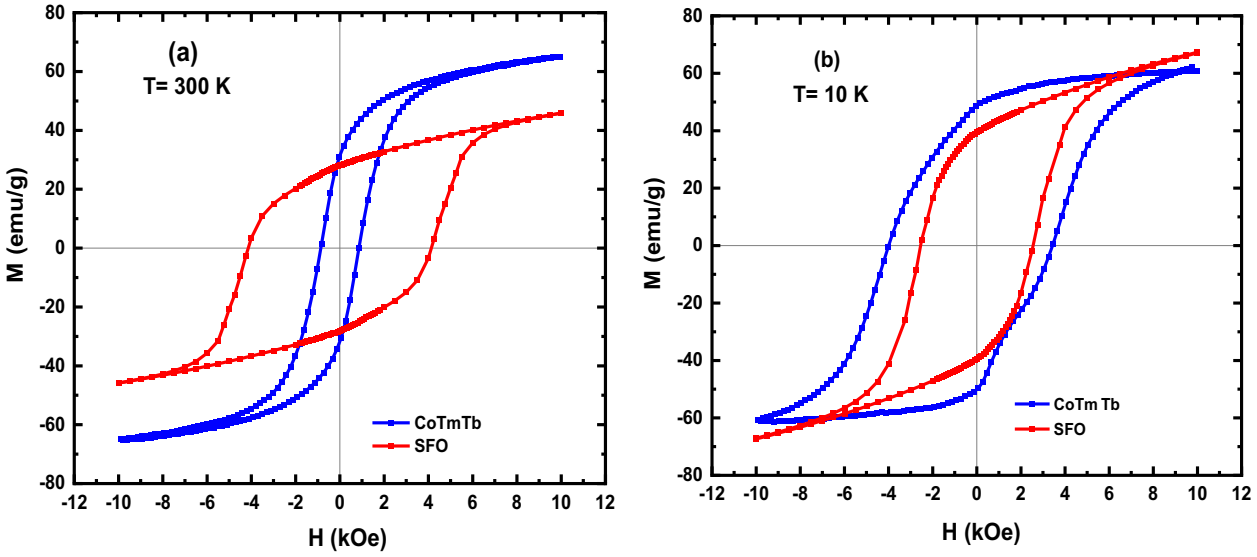

Fig. 7 M-H hysteresis loops for pure SFO hexaferrite and pure CoTmTb spinel ferrite samples registered at (a) T = 300 K and (b) T = 10 K.

by considering the effects of thermal fluctuations of the blocked moment across the anisotropy barrier. In our study, the magnetic hysteresis loops performed at room temperature indicate ferrimagnetic behavior for CoTmTb ferrite nanoparticles, indicating that the blocking temperature (T_B) is greatly higher than 300 K. For a system of non-interacting three-dimensional single domain magnetic NPs with uniaxial anisotropy, the temperature dependence of coercive field in the temperature range of (0–T_B K) can be expressed in the form of simple model of thermal activation of particle moments over the anisotropy barriers (knows as Kneller's law) as follows (Kneller and Hawig, 1991):

$$H_c(T) = H_c(0)\left[1 - \left(\frac{T}{T_B}\right)^{1/2}\right] \quad (3)$$

where $H_c(0)$ is the coercive field at T = 0 K. Accordingly, with decreasing the temperature, the coercivity will tend to increase. The observed magnetic properties for SFO and CoTmTb samples suggest that the combination of both of them into one sample could lead to develop exchange-coupled NCs products.

The evaluation of exchange-coupling behavior in SFO/x (CoTmTb) NCs products ($1.0 \leq x \leq 3.0$) was performed via analysis of magnetic measurements. Fig. 8 presents the *M-H* curves performed at RT and LT for various prepared NCs. The *M-H* curves at 300 K show smooth hysteresis loops without any kinks, which is the result of the coherent rotation of hard and soft spins with applied magnetic field (Kubelka, 1948). This behavior indicates the compatibility between the two phases and thus the achievement of a well-exchange coupling among the hard and soft phases. However, some kind of kinks was noticed in the *M-H* plots measured at LT, depicting individual switching of the hard and soft magnetic spins (Kubelka and Munk, 1931). This observation indicates a weakening of the exchange coupling behavior. This is mostly

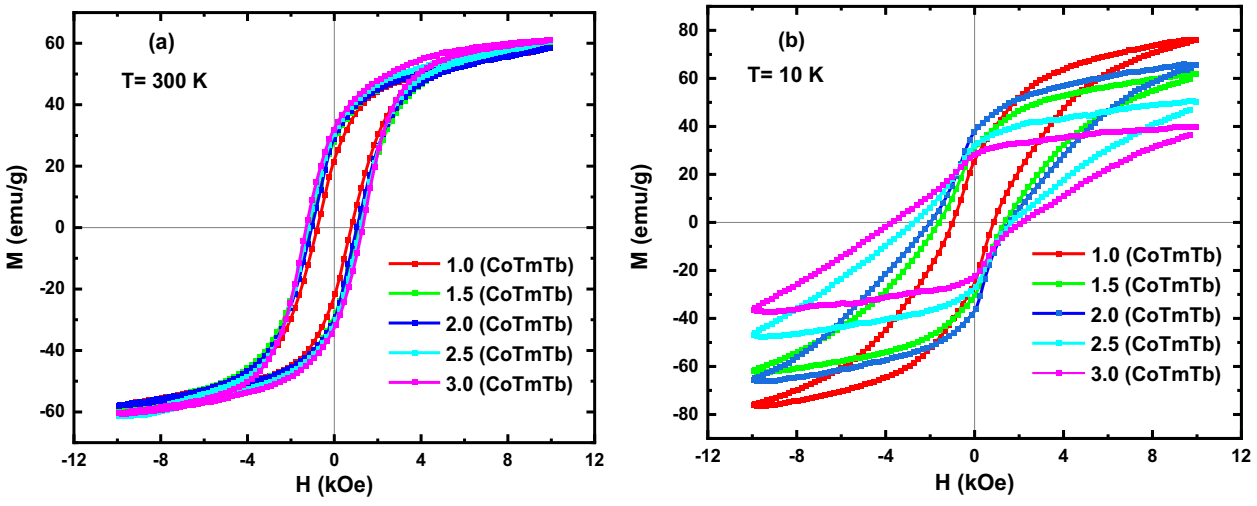

Fig. 8 The *M-H* hysteresis loops for the hard/soft SFO/x(CoTmTb) ($x \leq 3.0$) NCs performed at (a) T = 300 K and (b) T = 10 K.

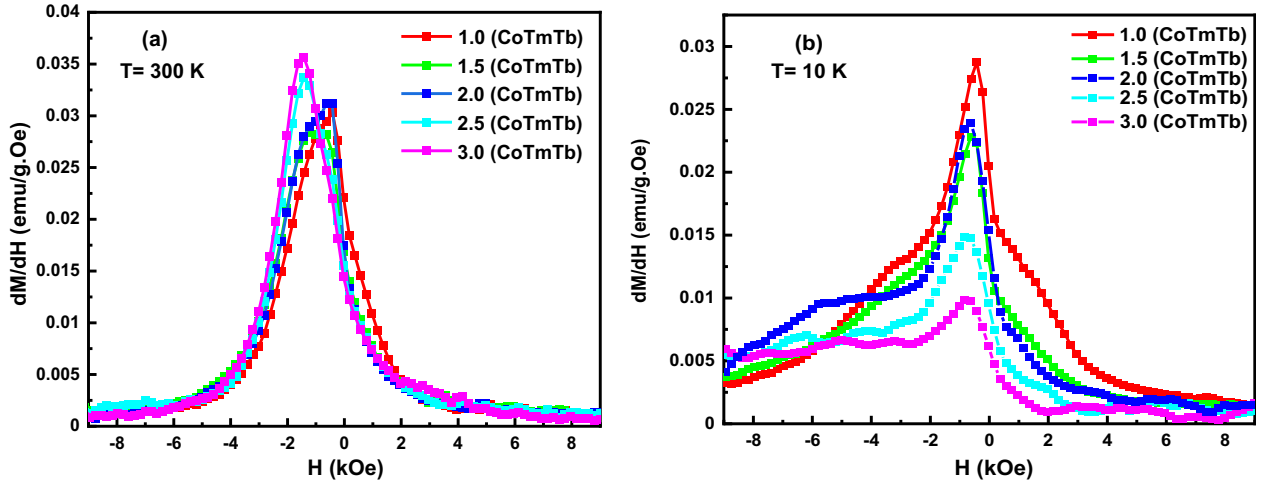

Fig. 9 The dM/dH versus H plots for the hard/soft SFO/x(CoTmTb) (x $\leq$ 3.0) NCs performed at (a) T = 300 K and (b) T = 10 K.

attributed to the inversement in the amplitudes of magnetic parameters with decreasing the temperature from RT to LT. Indeed, the pure soft phase (CoTmTb) displayed the highest M_s value and the pure hard phase (SFO) exhibits the largest coercivity at RT. However, at lower temperature, the lowest M_s and the largest coercivity is observed in the CoTmTb phase.

The strength of exchange-coupling between the hard and soft ferrite phases within various prepared NCs can be further evaluated by applying the derivation on the magnetization data with respects to H (Almessiere et al., 2019f). A single sharp peak was observed for all NCs at RT, confirming the strong exchange-coupling behavior between the two phases (Fig. 9a). At RT, the hard/soft SFO/3.0(CoTmTb) NCs showed the narrowest peak width and the highest intense peak among different produced NCs, which indicates the best exchange coupling in this product. However, an intense peak and small shoulder were observed in the measurements performed at 10 K, showing the weakening of exchange coupling behavior (Fig. 9b).

The various deduced magnetic parameters M_s, M_r, and H_c at RT and LT for the hard/soft SFO/x(CoTmTb) (x $\leq$ 3.0) NCs with respect to various amounts of soft phase content are listed in Tables 2 and 3, respectively. Fig. 10 shows the plots of M versus $1/H^2$ from which the M_s values were deduced. Generally, magnetic parameters are affected by many factors such as the distribution of both ferrites in the NCs, their average grain sizes, their particle shape, the strength of exchange coupling and dipolar interactions, and so on (Torkian et al., 2016; Pahwa et al., 2017; Almessiere et al., 2019e). At RT, different magnetic parameters (M_s, M_r, and H_c) show an enhancement in their values with increasing the soft phase content. One of the plausible reasons for this enhancement is the achievement of good exchange coupling effect between the hard and soft phases. Generally, the exchange-coupling interaction and dipolar interaction play a major role for the determination of magnetic properties of the composite magnets. According to the three-dimensional model proposed by Han et al. (2005), the hard and soft grains are in contact with each other and can be divided into two parts: an inner part without exchange-coupling interaction (uncoupled) and an interfacial part with exchange–coupling interaction (coupled). Therefore, the exchange-coupling interaction only influences the interface layer, which is basically equal to the exchange-length, and there is no exchange-coupling interaction in the inner part of grains. As the composite ferrite nanofibers are a mixture of the hard (SFO) and soft (NZFO) phases, there are three types of magnetic interactions. The major one is the interaction between soft-hard grains whereas the other two are the hard-hard and soft-soft. In the absence of absence of magnetic field, the spins are randomly oriented. Under an external magnetic field, most of spins are aligned in the direction of field in the case of pure hexaferrite. The hindered spins are not able to align because of the grain boundary hindrance to spin alignment in polycrystalline materials. These hindered spins may need higher field or an additional driving force to align. With the inclusion of CoTmTb soft ferrite phase, the interfacial spin interactions between

Table 2 Magnetic parameters for the hard/soft SFO/x(CoTmTb) (x $\leq$ 3.0) NCs at 300 K.

x	H_c (kOe)	M_r (emu/g)	M_s (emu/g)	SQR (M_r/M_s)	n_B (μ_B)
1.0	0.78	22.5	57.9	0.388	13.35
1.5	1.12	28.3	60.6	0.466	15.19
2.0	1.05	30.0	58.7	0.510	15.90
2.5	1.24	31.5	61.1	0.516	17.79
3.0	1.31	32.3	61.8	0.522	19.23

Table 3 Magnetic parameters for the hard/soft SFO/x(CoTmTb) (x $\leq$ 3.0) NCs at 10 K.

x	H_c (Oe)	M_r (emu/g)	M_s (emu/g)	SQR (M_r/M_s)	n_B (μ_B)
1.0	0.99	25.9	73.6	0.352	16.95
1.5	1.58	30.8	58.6	0.524	14.70
2.0	2.00	37.7	64.7	0.583	17.52
2.5	2.79	32.1	52.4	0.611	15.24
3.0	3.72	28.4	39.8	0.713	12.38

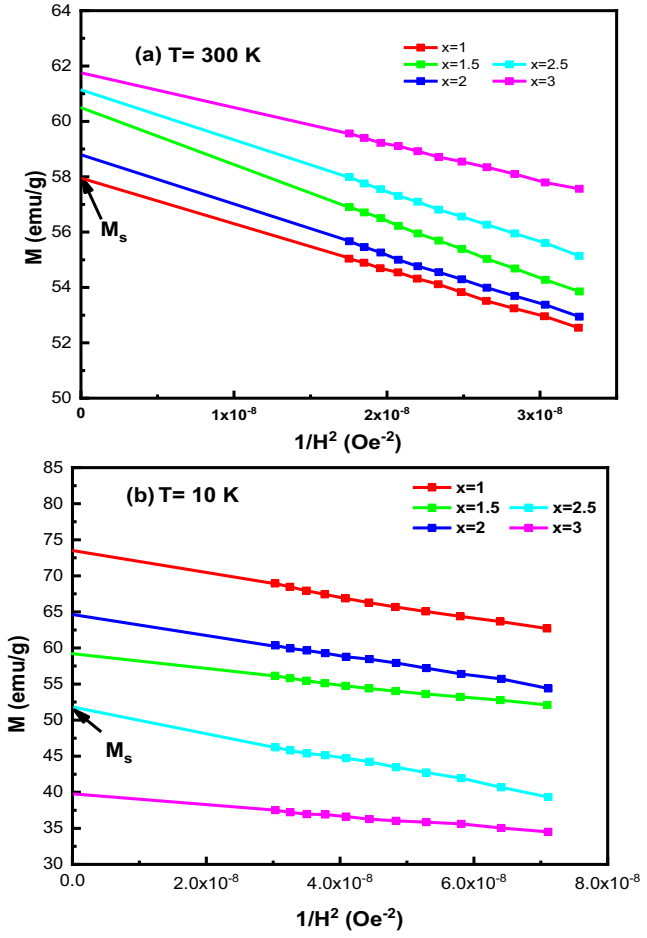

Fig. 10 M versus $1/H^2$ plots for different SFO/x(CoTmTb) NCs performed at (a) T = 300 K and (b) T = 10 K.

the hard and soft phases occur, which increase with the increase in soft phase content. Owing to the soft phase, the spins get swiftly align at much lower magnetic field and provide a torque to the hard-hindered spins. Consequently, higher fraction of spin alignment increases the magnetization (Pahwa et al., 2020; Almessiere et al., 2018a).

We note that the SFO ferrite display a high magneto-crystalline anisotropic energy in comparison to the soft CoTmTb phase. So, when a sufficient exchange-coupling is existing between the hard grains with the neighboring soft ferrite grains, the exchange-coupled interaction will not only align the magnetization in the soft ferrite grains but also make the magnetic moments of the interface of the SFO/CoTmTb nanocomposite deviating from the local easy axis and arrange in parallel with each other, which leads to a higher value of magnetization (Almessiere et al., 2018b; Song et al., 2012). Since the dipolar interaction is of a long-range phenomenon, it will be suppressed by the exchange-coupling interaction, resulting in an increase in magnetization with the mass ratio up to an optimal value. On other hand, according to the previous theoretical calculations (Han et al., 2005; Song et al., 2012), for effective exchange coupling, the size of hard grains should be greater than the size of soft grains by at least two times or more. In the current study, the sizes of hard SFO grains and soft CoTmTb grains within different prepared nanocomposite ferrites are in the range of 24.8–42.5 nm and of 60.5–81.5 nm, respectively, which are in line with the theoretical assumptions. This compatibility in the structure within the SFO/CoTmTb nanocomposite ferrites is helpful to achieve the strong exchange coupling. Consequently, the SFO/CoTmTb NCs could simultaneously combine the high saturation magnetization of soft phase and the large coercivity of hard phase, which is a key feature of the exchange-coupling behavior.

At low temperature (LT), it was found that the M_s decreases from 73.6 to 39.8 emu/g with increasing the spinel ferrite content. Contrarily, H_c is dramatically increased from 0.99 kOe in 1:1 NC to 3.72 kOe in 1:3 NC with spinel ferrite content rising. This behavior is attributed to the lower saturation magnetization and large coercivity in spinel ferrite phase compared to hard ferrite phase at LT.

The experimental values of magnetic moment (n_B) for various hard/soft SFO/x(CoTmTb) NCs in (the Bohr magneton μ_B unit) are calculated (Table 1 and 2) by using the following relationship (Algarou et al., 2020c; Algarou et al., 2020d):

$$n_B = \frac{M_w \times M_s}{5585} \tag{4}$$

where the term M_w indicates the molecular weight of the composite, and the '5585' constant is known as the magnetic factor. It is observed that the n_B value is increasing at RT with the increase in CoTmTb content, whereas it is decreasing at LT. This tendency is good agreement with that of M_s values.

According to our results, the good exchange-coupling behavior and highest magnetic parameters (i.e. high saturation and large coercivity) are detected for the hard/soft SFO/x (CoTmTb) NCs with the mass ratio of 1:3 at measured temperature of 300 K. Therefore, we interested to determine the maximum energy product $(BH)_{max}$ for all products at RT. $(BH)_{max}$ value is estimated by converting the M-H hysteresis loop to B-H hysteresis curve using the following equation (Fischbacher et al., 2018; Yang et al., 2016):

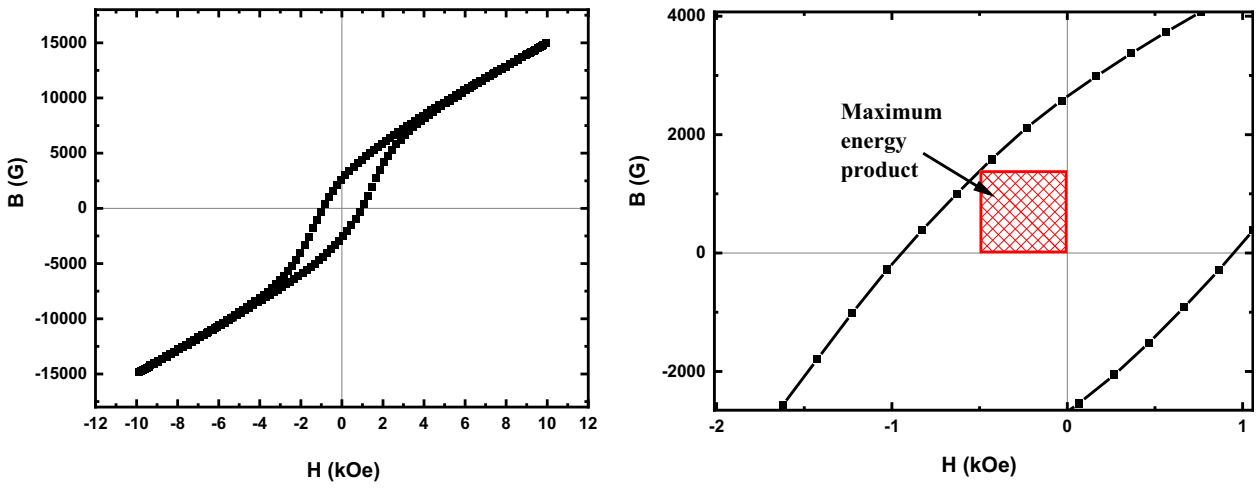

Fig. 11 Example of B versus H curve for the hard/soft SFO/x(CoTmTb) (x = 3.0) NCs performed at T = 300 K.

$$B = H + 4\pi M \quad (5)$$

The largest rectangle area in the second quadrant of *B-H* curve lead to determine the $(BH)_{max}$ value as shown in Fig. 11. $(BH)_{max}$ values are found to be equal to 0.21 MGOe (=1.66 kJ/m^3), 0.49 MGOe (=3.93 kJ/m^3), 0.42 MGOe (=3.31 kJ/m^3), 0.66 MGOe (=5.23 kJ/m^3), and 0.71 MGOe (=5.65 kJ/m^3) for 1:1, 1:1.5, 1:2, 1:2.5, and 1:3, respectively. $(BH)_{max}$ increases and reaches its maximum for SFO/3 (CoTmTb) NC. The obtained $(BH)_{max}$ value in this NC is higher than those reported previously in SFO formed by ball milling method (Abraime et al., 2017; Stingaciu et al., 2015), NCs of $(BaFe_{12}O_{19})_{1-x}/(Ni_{0.6}Zn_{0.4}Fe_2O_4)_x$ ($x \leq 0.3$) prepared by physical mixing approach (Nikmanesh et al., 2017), $BaFe_{12}O_{19}/CoFe_2O_4$ composite at the mass ratio (0.6:0.4) synthesized via sol–gel process (Yang et al., 2015), and $BaFe_{12}O_{19}/MgFe_2O_4$ fabricated through co-precipitation and ultrasonic techniques and calcinated at 600 °C (Hoque et al., 2013). The obtained result suggests the possibility to use hard/soft SFO/x(CoTmTb) ($x \leq 3.0$) NCs for permanent magnet and magnetic recording applications. \

3.5. Microwave properties

Using Nicholson-Ross-Weir approach frequency dispersions of the μ and ε (real and imaginary parts) were calculated from S11 and S21 parameters (Klygach et al., 2017; Vinnik et al., 2018). All features of the used set up are in (Klygach et al., 2018). The transmission line with waveguide was used for the electrodynamic property measurements.

Figs. 12–13 show the frequency dispersions of the ε and μ (real and imaginary parts) of the samples. The dipole polarization, which determines the value of ε', is result of the influence of the external electric field on electrical dipoles in material (field orients of the electrical dipoles). This leads to rise of the losses for overcoming the coupling forces.

Dielectric losses are determined by the ε'' (imaginary part) at lower frequencies, when dipole polarization prevails. With increasing frequency, the dipole polarization goes over to ion-relaxation. This can be seen in the frequency range 38–46 GHz. The changes of the real part of ε' (with the minimum at a frequency of 41 GHz) confirm the mechanism of transfor-

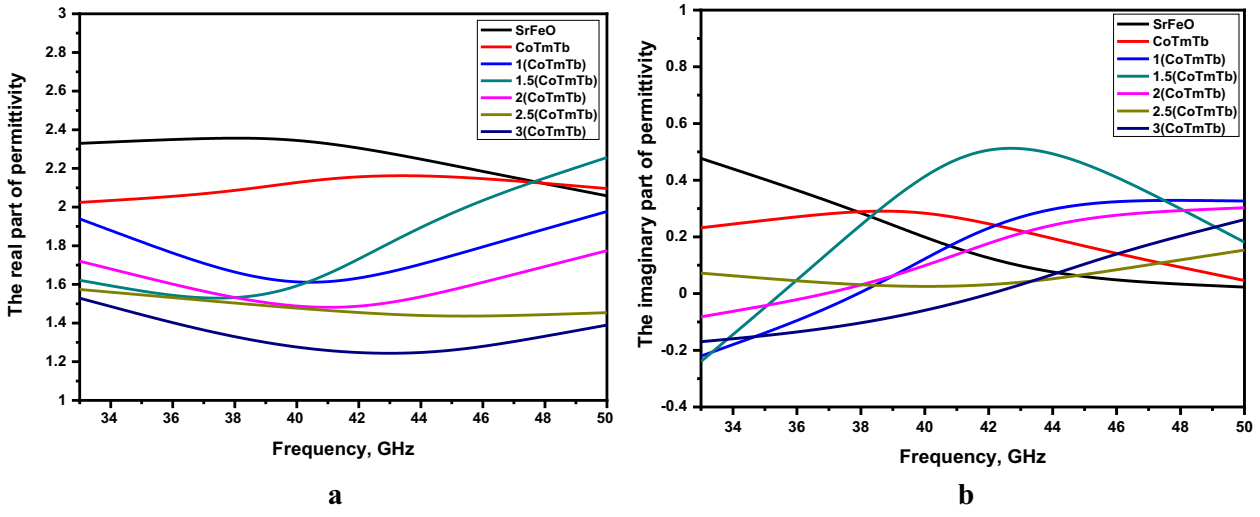

Fig. 12 The frequency dispersions of the ε′ (a) and ε″ (b) of the hard/soft SFO/x(CoTmTb) ($x \leq 3.0$) NCs.

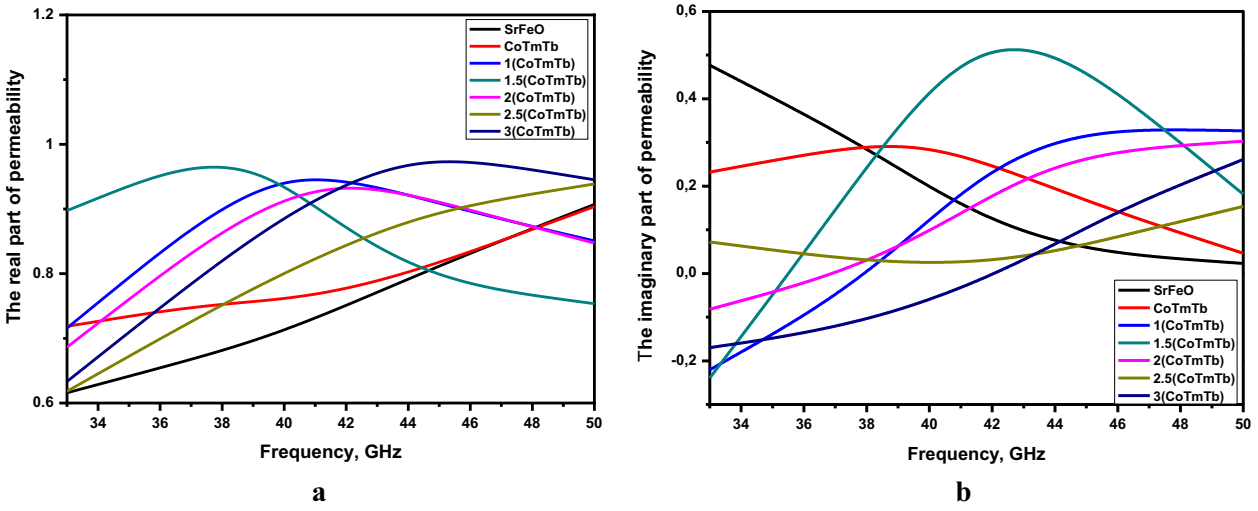

Fig. 13 Frequency dispersions of the μ′ (a) and μ′ (b) of the hard/soft SFO/x(CoTmTb) (x ≤ 3.0) NCs.

mation. As this transition proceeds, the losses decrease, which is expressed in a decrease in the absolute value of ε'' (Fig. 12b).

Since the loss in all substances decreases during the transition to ion-relaxation polarization, the values of the $-\varepsilon''$ in modulus generally decrease in all samples of the material (Figs. 12b, 13b). This indirectly confirms the above conclusion about the observed transition from dipole to ion-relaxation polarization. The frequency of the dipole orientation does not have time to the change with frequency increasing.

As a result, the polarization of the dipoles transforms into ion-relaxation polarization. This mechanism (ion-relaxation polarization) can be described as displacement of ions at the sites of the unit cell, or located between the sites.

The magnetic permeability of the composites has features in the same frequency ranges as the dielectric (Fig. 13).

In the material, magnetic moments are fluctuated (spin precession) so that the magnetic moment of each atom is compensated. Internal magnetic field (in material) induces the weak induction currents (according to Faraday's law). Magnetic flux generated by these currents with opposite direction to the external magnetic field (according to Lenz's law). As a consequence of this, the value of μ' (real part) will practically no change in frequency and μ'≈1.

All investigated samples of the substance behave like paramagnets, for such materials μ ≤ 1. Since the components of the mixture are also paramagnetic. The change in magnetic permeability with frequency can be explained using a Larmor's theorem. Since in a quiescent state, samples of a substance have their own magnetic moment, which is of little value and does not significantly affect the overall value of the magnetic permeability of the composite. When a substance is placed in an external alternating magnetic field, according to the Larmor's theorem, the precession of the magnetic moment of electrons begins.

The increase in modulus of μ'' (imaginary part) (Fig. 13b) can be explained as follows. An increase in frequency results a rise in the precession of the magnetic moment of electrons and an increase in the energy expended to maintain the precession, i.e. losses. The features of the different types of polarization and conditions for their transformation demonstrated in Fig. 14.

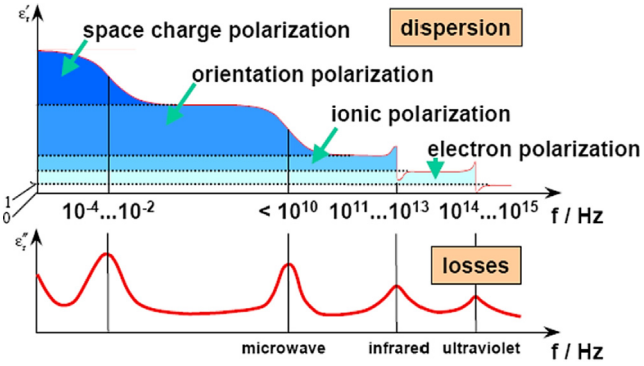

Fig.14 Frequency dependences of the different types of polarization.

Electrodynamic parameters (frequency dispersions of the permeability and permittivity) were used for calculation of the reflection losses (R) in accordance with following equation:

$$R = \frac{i\sqrt{\frac{\dot{\mu}_2}{\dot{\varepsilon}_2}}tg\left(\dot{k}_2 d\right) - 1}{i\sqrt{\frac{\dot{\mu}_2}{\dot{\varepsilon}_2}}tg\left(\dot{k}_2 d\right) + 1} \quad (6)$$

where

$\dot{k}_2$ – complex wavenumber ($\dot{k}_2 = \omega\sqrt{\dot{\varepsilon}_2\dot{\mu}_2}$),
d – layer thickness.

Using Eq. (6) we calculated the R for SFO/x(CoTmTb) (x ≤ 3.0) NCs with different thickness. Fig. 15 demonstrates frequency dispersions of the R in the 33–50 GHz range. For pure compositions (SFO and CoTmTb), it can be seen that with an increase in the material layer, the dependence of the reflection coefficient rapidly tends to the values for an infinite layer. With a layer thickness of 24 mm, the dependences practically do not differ from each other with an increase in the layer. This is explained by the fact that the depth of the skin layer is small and the wave amplitude decays very quickly. For various compositions of material samples at low values

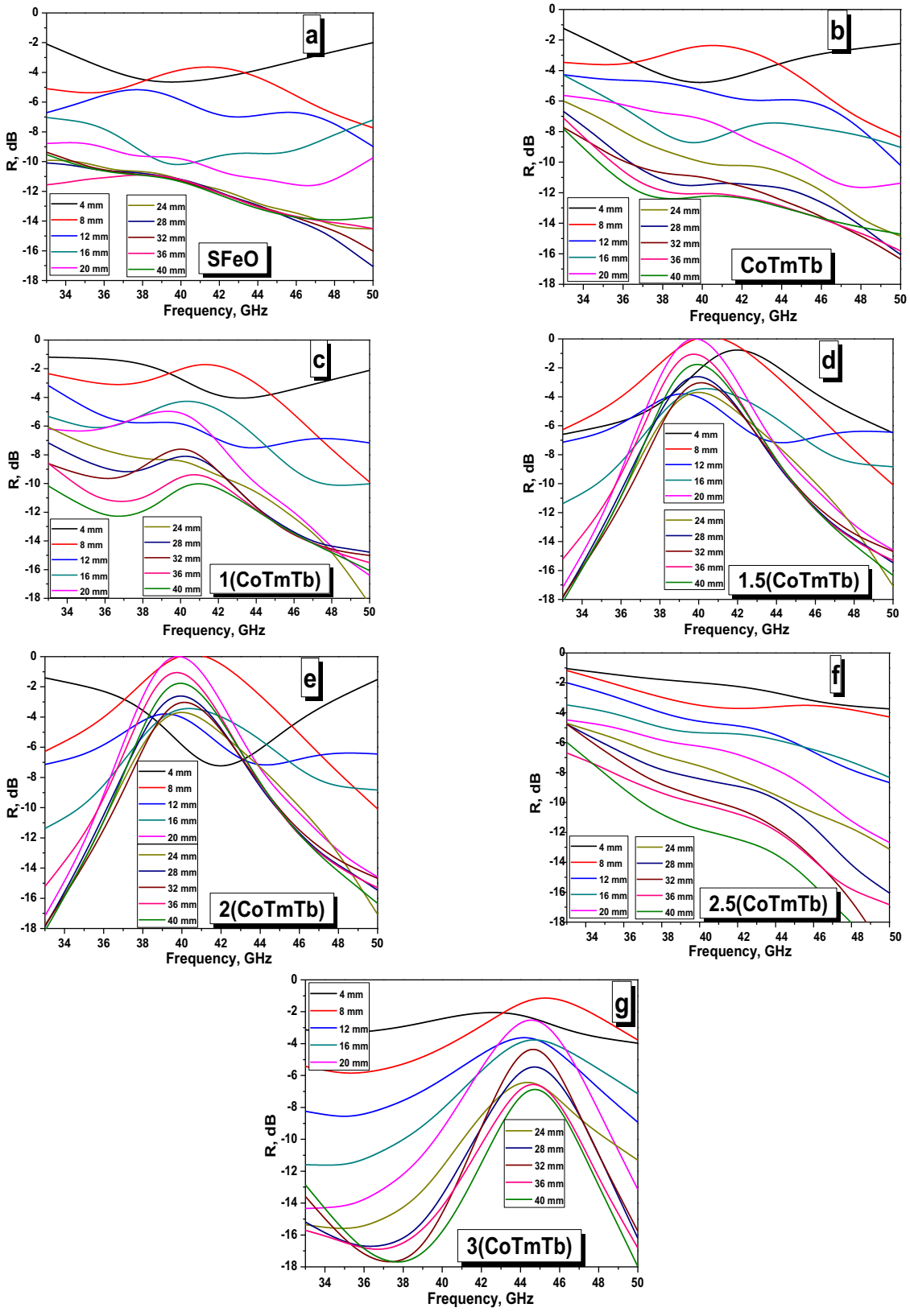

Fig. 15 Calculated frequency dispersions of the R for the hard/soft SFO/x(CoTmTb) NCs with different thickness (4–40 mm): SFO (a); CoTmTb (b); SFO/1(CoTmTb) (c); SFO/1.5(CoTmTb) (d); SFO/2(CoTmTb) (e); SFO/2.5(CoTmTb) (f) and SFO/3(CoTmTb) (g).

of the CoTmTb concentration, the dependences, with an increase in the thickness of the material layer, tend to the values for infinite as quickly, with an increase in the layer thickness. As the concentration rises, a resonance is seen, which is expressed by the fact that at certain frequencies the reflection coefficient is practically equal to 0, i.e. the full reflection from the material layer occurs. With concentration increasing, resonance shifts to high frequencies. This is due to wave interference, which is confirmed by the fact that along with the maximum points of the reflection coefficient, there are minimum points.

4. Conclusion

The hard/soft ferrite nanocomposites that comprised of the SFO as a hard phase and x(CoTmTb) ($x \leq 3.0$) for spinel phase where synthesized effectively thru *one-pot* citrate combustion approach. The coexisting of both hard and soft phase was confirmed by XRD, TEM and HR-TEM. The average crystal size of the SFO was found about 53% larger than the CoTmTb. The surface analysis of the hard/soft NCs showed the big hexagonal platelets particles coated by accumulation of small cubic particles. The same order of light absorption intensities and band gap magnitudes are observed for hard/soft NCs and CoTmTb spinel sample. Both type of samples has E_g values in a narrow range of 1.32–1.47 eV, while SFO NPs have higher direct band gap value of 1.79 eV. This means determined E_g values are in the semiconductor s band gap order for all samples. The magnetic properties for various NCs were also inspected via measurements of magnetization (M) against applied magnetic field (H) performed at two different temperatures 300 K (RT) and 10 K (LT). At RT, the different NCs display good magnetic properties and good exchange coupling behavior as revealed by the investigation of M vs H loops and dM/dH vs H plots. The various magnetic parameters including M_s, M_r, H_c, and $(BH)_{max}$ showed an improvement in their values with the increase of the soft content. Accordingly, the studied hard/soft NCs could be useful as permanent magnets and magnetic recording media. Microwave properties were measured in the frequency range 33–50 GHz using waveguide method. Frequency dispersions of the real/imaginary parts of permittivity and permeability were calculated from S-parameters. Non-linear behavior of the microwave characteristics for the SFO/x(CoTmTb) composites with different ratio 1: x between the hexaferrite phase (SFO) and spinel phase (CoTmTb) was observed. Energy losses for investigated composites associated with the different types of polarization losses. Phenomena of the resonant absorption were not observed in this frequency range. Strong coupling between soft and hard magnetic phase can be used for developing of the functional media for high-frequency devices such as circulators, phase-shifters and inventors. The calculated reflection losses for SFO/x(CoTmTb) NCs demonstrated strong correlation between the thickness of the layer (4–40 mm) and with composition (ratio between hard and soft phases).

Declaration of Competing Interest

The authors declare that they have no known competing financial interests or personal relationships that could have appeared to influence the work reported in this paper.

Acknowledgements

This work was financially supported by the Deanship for Scientific Research (Project application No. 2020-164-IRMC) of Imam Abdulrahman Bin Faisal University (IAU – Saudi Arabia). Microwave characterization was partially supported by the Russian Science Foundation (Agreement No. 19-72-10071 from 06 Aug. 2019).

References

Abraime, B., Tamerd, M.A., Mahmoud, A., Boschini, F., Benyoussef, A., Hamedoun, M., Xiao, Y., El Kenz, A., Mounkachi, O., 2017. Experimental and theoretical investigation of SrFe12O19 nanopowder for permanent magnet application. Ceram. Int. 43, 15999–16006.

Algarou, N.A., Slimani, Y., Almessiere, M.A., Baykal, A., 2020a. Exchange-coupling behavior in SrTb0.01Tm0.01Fe11.98O19/(CoFe2O4)x hard/soft nanocomposites. New J. Chem. 44, 5800–5808.

Algarou, N.A., Slimani, Y., Almessiere, M.A., Rehman, S., Younas, M., Unal, B., Demir Korkmaz, A., Gondal, M.A., Trukhanov, A. V., Baykal, A., Nahvi, I., 2020b. Developing the magnetic, dielectric and anticandidal characteristics of SrFe12O19/(Mg0.5Cd0.5Dy0.03Fe1.97O4)x hard/soft ferrite nanocomposites. J. Taiwan. Inst. Chem. Eng. 113, 344–362.

Algarou, N.A., Slimani, Y., Almessiere, M.A., Baykal, A., Guner, S., Manikandan, A., Ercan, I., 2020c. Enhancement on the exchange coupling behavior of SrCo0.02Zr0.02Fe11.96O19/MFe2O4 (M = Co, Ni, Cu, Mn and Zn) as hard/soft magnetic nanocomposites. J. Magn. Magn. Mater. 499, 166308.

Algarou, N.A., Slimani, Y., Almessiere, M.A., Güner, S., Baykal, A., Ercan, I., Kögerler, P., 2020d. Exchange-coupling effect in hard/soft SrTb0.01Tm0.01Fe11.98O19/AFe2O4 (where A = Co, Ni, Zn, Cu and Mn) composites. Ceram. Int. 46 (6), 7089–7098.

Almessiere, M., Sözeri, H., Trukhanov, A., Slimani, Y., Ali, S., Acar, E., Baykal, A., 2019a. Tb3+ ion substituted Sr-hexaferrites as high quality microwave absorbers. J. Magn. Magn. Mat. 491, 165595.

Almessiere, M., Slimani, Y., Tashkandi, N., Güngüneş, H., Sertkol, M., Nawaz, M., Ali, S., Baykal, A., Ercan, I., 2019b. Tailored microstructures, optical and magnetic qualities of strontium hexaferrites: Consequence of Tm3+ and Tb3+ ions Co-substitution. Ceram. Int. 45, 21385–21394.

Almessiere, M.A., Slimani, Y., Korkmaz, A.D., Guner, S., Sertkol, M., Shirsath, S.E., Baykal, A., 2019c. Sonochemical synthesis and physical properties of Co0.3Ni0.5Mn0.2EuxFe2-xO4 nano-spinel ferrites. Ultrason-Sonochem. 54, 1–10.

Almessiere, M.A., Slimani, Y., Korkmaz, A.D., Guner, S., Sertkol, M., Shirsath, S.E., Baykal, A., 2019d. Structural, optical and magnetic properties of Tm3+ substituted cobalt spinel ferrites synthesized via sonochemical approach. Ultrason. Sonochem. 54, 11–20.

Almessiere, M.A., Slimani, Y., Korkmaz, A.D., Baykal, A., Güngüneş, H., Sözeri, H., Shirsath, S.E., Güner, S., Akhtar, S., Manikandan, A., 2019e. Impact of La3+ and Y3+ ion substitutions on structural, magnetic and microwave properties of Ni0.3Cu0.3Zn0.4Fe2O4 nanospinel ferrites synthesized via sonochemical route. RSC Adv. 9, 30671–30684.

Almessiere, M.A., Slimani, Y., Ali, S., Baykal, A., Ercan, I., Sozeri, H., 2019f. Nd3+ Ion-substituted Co1−2xNixMnxFe2−yNdyO4 nanoparticles: Structural, morphological, and magnetic investigations. J. Inorg. Organ. Polym. Mater. 29, 783–791.

Almessiere, M.A., Slimani, Y., Auwal, I.A., Shirsath, S.E., Manikandan, A., Baykal, A., Özçelik, B., Ercan, I., Trukhanov, S.V., Vinnik, D.A., Trukhanov, A.V., 2020. Impact of Tm3+ and Tb3+

rare earth cations substitution on the structure and magnetic parameters of Co-Ni nanospinel ferrite. Nanomaterials 10, 2384.
Almessiere, M.A., Slimani, Y., Baykal, A., 2018a. Exchange spring magnetic behavior of Sr0.3Ba0.4Pb0.3Fe12O19/(CuFe2O4)x nanocomposites fabricated by a one-pot citrate sol-gel combustion method. J. Alloys Compd. 762, 389–397.
Almessiere, M.A., Slimani, Y., Baykal, A., 2018b. Structural, morphological and magnetic properties of hard/soft SrFe12-xVxO19/(Ni0.5Mn0.5Fe2O4)y nanocomposites: Effect of vanadium substitution. J. Alloys Compd. 767, 966–975.
Auwal, I.A., Baykal, A., Güner, S., Sertkol, M., Sözeri, H., 2016a. Magneto-optical properties BaBixLaxFe12−2xO19 (0.0≤x≤0.5) hexaferrites. J. Magn. Magn. Mater. 409, 92–98.
Auwal, I.A., Güngüneş, H., Güner, S., Shirsath, S.E., Sertkol, M., Baykal, A., 2016b. Structural, magneto-optical properties and cation distribution of SrBixLaxYxFe12− 3xO19 (0.0≤ x≤ 0.33) hexaferrites. Mater. Res. Bull. 80, 263–272.
Auwal, I.A., Güner, S., Güngüneş, H., Baykal, A., 2016c. Sr1-xLaxFe12O19 (0.0≤x≤0.5) hexaferrites: Synthesis, characterizations, hyperfine interactions and magneto-optical properties. Ceram. Int. 42 (11), 12995–13003.
Auwal, I.A., Baykal, A., Güner, S., Sözeri, H., 2017. Magneto-optical properties of SrBixLaxFe12-2xO19 (0.0≤x≤0.5) hexaferrites by sol-gel auto-combustion technique. Ceram. Int. 43, 1298–1303.
Auwal, I.A., Güngüneş, H., Baykal, A., Güner, S., Shirsath, S.E., Sertkol, M., 2016d. Structural, morphological, optical, cation distribution and Mössbauer analysis of Bi3+ substituted strontium hexaferrite. Ceram. Int. 42 (7), 8627–8635.
Baykal, A., Auwal, I., Güner, S., Sözeri, H., 2017. Magnetic and optical properties of Zn2+ ion substituted barium hexaferrites. J. Magn. Magn. Mat. 430, 29–35.
Doma, R., Borse, P.H., Cho, C.R., Lee, J.S., Yu, S.M., Yoon, J.H., Hong, T.E., Jeong, E.D., Kim, H.G., 2012. Synthesis of SrFe12O19 and Sr7Fe10O22 systems for visible light photocatalytic studies. J. Ceram. Process. Res. 13, 451–456.
Fischbacher, J., Kovacs, A., Gusenbauer, M., Oezelt, H., Exl, L., Bance, S., Schrefl, T., 2018. Micromagnetics of rare-earth efficient permanent magnets. J. Phys. D: Appl. Phys. 51, 193002.
Gharibshahi, E., Young, B.D., Bhalla, A.S., Guo, R., 2020. Theory, simulation and experiment of optical properties of cobalt ferrite (CoFe2O4) nanoparticles. J. Mater. Sci. Technol. 57, 180–187.
Ghimire, M.L., Kunwar, D.L., Dahal, J.N., Neupane, D., Yoon, S., Mishra, S.R., 2020. Co-doped rare-Earth (La, Pr) and Co-Al substituted M-type strontium hexaferrite: structural, magnetic, and Mossbauer spectroscopy study. Mat. Sci. Appl. 11, 474–493.
González-Angeles, A., Mendoza-Suárez, G., Grusková, A., Dosoudil, R., Ortega-Zempoalteca, R., 2004. Magnetic studies of Sn2+–Sn4+-substituted barium hexaferrites synthesized by mechanical alloying. Mat. Lett. 58, 2906–2910.
Güner, S., Almessiere, M.A., Slimani, Y., Baykal, A., Ercan, I., 2020. Microstructure, magnetic and optical properties of Nb3+ and Y3+ ions co-substituted Sr hexaferrites. Ceram. Int. 46 (4), 4610–4618.
Harris, V.G., 2011. Modern microwave ferrites. IEEE Trans. Magn. 48, 1075–1104.
Harikrishnan, V., Ezhil, R., Vizhi, 2016. A study on the extent of exchange coupling between (Ba0.5Sr0.5Fe12O19)1–x(CoFe2O4)x magnetic nanocomposites synthesized by solgel combustion method. Magn. Magn. Mater. 418, 217–223.
Han, Q.X., Meng, X.F., Lu, C.H., 2018. Exchange-coupled Ni0.5Zn0.5Fe2O4/SrFe12O19 composites with enhanced microwave absorption performance. J. Alloys Compd. 768, 742–749.
Han, G.B., Gao, R.W., Fu, S., Feng, W.C., Liu, H.Q., Chen, W., Li, W., Guo, Y.Q., 2005. Appl. Phys. A 81, 579–582.
Hazra, S., Ghosh, B.K., Patra, M.K., Jani, R.K., Vadera, S.R., Ghosh, N.N., 2015. A novel 'one-pot' synthetic method for preparation of (Ni0.65Zn0.35Fe2O4)x–(BaFe12O19)1–x nanocomposites and study of their microwave absorption and magnetic properties. Powder Technol. 279, 10–17.
Hilczer, A., Kowalska, K., Markiewicz, E., Pietraszko, A., Andrzejewski, B., 2016. Dielectric and magnetic response of SrFe12O19–CoFe2O4 composites obtained by solid state reaction. Mat. Sci. Eng. B 207, 47–55.
Hoque, S.M., Srivastava, C., Kumar, V., Venkatesh, N., Das, H.N., Saha, D.K., Chattopadhyay, K., 2013. Exchange-spring mechanism of soft and hard ferrite nanocomposites. Mater. Res. Bull. 48, 2871–2877.
Javidan, A., Rafizadeh, S., Hosseinpour-Mashkani, S.M., 2014. Strontium ferrite nanoparticle study: Thermal decomposition synthesis, characterization and optical and magnetic properties. Mater. Sci. Semicond. Process 27, 468–473.
Josh, S., Kumar, M., Pandey, H., Chhoker, S. 2019. Optical properties of Gd3+ substituted CoFe2O4 nanoparticles. AIP Conf. Proc. 2136, 040007.
Khandani, M., Yousefi, M., Afghahi, S., Amini, M., Torbati, M.B., 2019. An investigation of structural and magnetic properties of Ce–Nd doped strontium hexaferrite nanoparticles as a microwave absorbent. Mat. Chem. Phys. 235, 121722.
Klygach, D.S., Vakhitov, M.G., Zherebtsov, D.A., Kudryavtsev, O. A., Knyazev, N.S., Malkin, A.I., 2017. Investigation of electrical parameters of corundum-based material in X-band. J. Mater. Sci: Mater. Electron. 28 (18), 13621–13625.
Klygach, D.S., Vakhitov, M.G., Vinnik, D.A., Bezborodov, A.V., Gudkova, S.A., Zhivulin, V.E., Zherebtsov, D.A., SakthiDharan, C.P., Trukhanov, S.V., Trukhanov, A.V., Starikov, A.Y., 2018. Measurement of permittivity and permeability of barium hexaferrite. J. Magn. Magn. Mater. 465, 290–294.
Kneller, E.F., Hawig, R., 1991. The exchange-spring magnet: a new material principle for permanent magnets. IEEE Trans. Magn. 27, 3588–3600.
Kubelka, P., 1948. New contributions to the optics of intensely light-scattering materials. Part I. J. Opt. Soc. Am. 38, 448–457.
Kubelka, P., Munk, F., 1931. Ein Beitrag Zur Optik Der Farbanstriche. Z. Tech. Phys. 12, 593–601.
Kumar, A., Agarwala, V., Singh, D., 2013. Effect of particle size of BaFe12O19 on the microwave absorptioncharacterıstıcs in X-band. Prog. In Electromag. Res. 29, 223–236.
Mameli, V., Angotzi, M.S., Cara, C., Cannas, C., 2019. Liquid phase synthesis of nanostructured spinel ferrites-A review. J. Nanosci. Nanotechnol. 19, 4857–4887.
Mehdipour, M., Shokrollahi, H., 2013. Comparison of microwave absorption properties of SrFe12O19, SrFe12O19/NiFe2O4, and NiFe2O4 particles. J. Appl. Phys. 114, 043906.
Meng, X.F., Hana, Q.X., Sun, Y.J., Liu, Y.F., 2019. Synthesis and microwave absorption properties of Ni0.5Zn0.5Fe2O4/BaFe12O19@polyaniline composite. Ceram. Int. 45, 2504–2508.
Mousavi Ghahfarokhi, S.E., Ahmadi, M., Kazeminezhad, I., 2020. Fabrication of the SrFe11MnO19/CoFe1.9Bi0.1O4 ferrite nanocomposite and investigation the properties of its microwave absorption in X-band. Phys. B 594, 412290.
Nikmanesh, H., Moradi, M., Kameli, P., Bordbar, G.H., 2017. Effects of annealing temperature on exchange spring behavior of barium hexaferrite/nickel zinc ferrite nanocomposites. J. Electron. Mater. 46, 5933–5941.
Pahwa, C., Narang, S.B., Sharma, P., 2020. Composition dependent magnetic and microwave properties of exchange-coupled hard/soft nanocomposite ferrite. J. Alloy Compd. 815, 152391.
Pahwa, C., Mahadevan, S., Narang, S.B., Sharma, P., 2017. Structural, magnetic and microwave properties of exchange coupled and non-exchange coupled BaFe12O19/NiFe2O4 nanocomposites. J. Alloys Compd. 725, 1175–1181.
Radmanesh, M.A., Seyyed Ebrahimi, S.A., 2012. Synthesis and magnetic properties of hard/soft SrFe12O19/Ni0.7Zn0.3Fe2O4 nanocomposite magnets. J. Magn. Magn. Mater. 324, 3094–3098.

Sadaqat, A., Almessiere, M., Slimani, Y., Guner, S., Sertkol, M., Albetran, H., Baykal, A., Shirsath, S.E., Ozcelik, B., Ercan, I., 2019. Structural, optical and magnetic properties of Tb3+ substituted Co nanoferrites prepared via sonochemical approach. Ceram. Int. 45 (17), 22538–22546.

Singh, V.P., Jasrotia, R., Kumar, R., Raizada, P., Thakur, S., Batoo, K.M., Singh, M., 2018. A current review on the synthesis and magnetic properties of M-type hexaferrites material. World J. of Cond. Mat. Phys. 8, 36.

Shams, M.H., Rozatian, A.S., Yousefi, M.H., Valícek, J., Sepelak, V., 2016. Effect of Mg^{2+} and Ti^{4+} dopants on the structural, magnetic and high-frequency ferromagnetic properties of barium hexaferrite. J. Magn. Magn. Mater 399, 10–18.

Stingaciu, M., Topole, M., Mcguiness, P., Christensen, M., 2015. Magnetic properties of ball-milled SrFe12O19 particles consolidated by Spark-plasma sintering. Sci. Rep. 5, 1–8.

Song, F.Z., Shen, X.Q., Liu, M.Q., Xiang, J., 2011. Magnetic hard/soft nanocomposite ferrite aligned hollow microfibers and remanence enhancement. J. Colloid. Interf. Sci. 354, 413–416.

Song, F.Z., Shen, X.Q., Liu, M.Q., Xiang, J., 2012. Microstructure, magnetic properties and exchange–coupling interactions for one-dimensional hard/soft ferrite nanofibers. J. Solid State Chem. 185, 31–36.

Tauc, J., Grigorovici, R., Vancu, A., 1966. Optical properties and electronic structure of amorphous germanium. Phys. Status Solidi. 15, 627–637.

Thakur, P., Chahar, D., Taneja, S., Bhalla, N., Thakur, A., 2020. A review on MnZn ferrites: Synthesis, characterization and applications. Ceram. Int. 46, 15740–15763.

Torkian, S., Ghasemi, A., Razavi, R.S., 2016. Magnetic properties of hard-soft SrFe10Al2O19/Co0.8Ni0.2Fe2O4 ferrite synthesized by one-pot sol–gel auto-combustion. J. Magn Magn. Mat. 416, 408–416.

Tong, G., Liu, Y., Cui, T., Li, Y., Zhao, Y., Guan, J., 2016. Tunable dielectric properties and excellent microwave absorbing properties of elliptical Fe_3O_4 nanorings. Appl. Phys. Lett. 108, 072905.

Topkaya, R., 2017. Effect of Zn substitution on temperature dependent magnetic properties of $BaFe_{12}O_{19}$ hexaferrites. J. Alloys Compd. 725, 1230–1237.

Trukhanov, S., Trukhanov, A., Kostishyn, V., Panina, L., Trukhanov, A.V., Turchenko, V., Tishkevich, D., Trukhanova, E., Yakovenko, O., Matzui, L.Y., 2017. Effect of gallium doping on electromagnetic properties of barium hexaferrite. J. Phys. Chem. Sol. 111, 142–152.

Trukhanov, S., Trukhanov, A., Salem, M., Trukhanova, E., Panina, L., Kostishyn, V., Darwish, M., Trukhanov, A.V., Zubar, T., Tishkevich, D., 2018. Preparation and investigation of structure, magnetic and dielectric properties of (BaFe11.9Al0.1O19)1-x-(BaTiO3)x bicomponent ceramics. Ceram. Int. 44, 21295–21302.

Vinnik, D., Podgornov, F., Zabeivorota, N., Trofimov, E., Zhivulin, V., Chernukha, A., Gavrilyak, M., Gudkova, S., Zherebtsov, D., Ryabov, A., 2020. Effect of treatment conditions on structure and magnetodielectric properties of barium hexaferrites. J. Magn. Magn. Mat. 498, 166190.

Vinnik, D.A., Klygach, D.S., Zhivulin, V.E., Malkin, A.I., Vakhitov, M.G., Gudkova, S.A., Galimov, D.M., Zherebtsov, D.A., Trofimov, E.A., Knyazev, N.S., Atuchin, V.V., Trukhanov, S.V., Trukhanov, A.V., 2018. Electromagnetic properties of BaFe12O19: Ti at centimeter wavelengths. J. Alloys Compd. 755, 177–183.

Wang, J., Zhou, H., Zhuang, J., Liu, Q., 2015. Magnetic γ-Fe2O3, Fe3O4, and Fe nanoparticles confined within ordered mesoporous carbons as efficient microwave absorbers. Phys. Chem. Chem. Phys. 17, 3802–3812.

Wang, L., Yu, G., Zhu, C., Lv, F., Liu, F., Kong, W., 2019. Preparation and investigation of structure, magnetic, and dielectric properties of (1–x)Bi2Fe4O9–xMgFe2O4 bicomponent ceramics. J. Mater. Sci.: Mater Electron. 30, 20556–20565.

Xia, J.Y., Ning, Y., Luo, Y.H., Chen, W., Wu, X.H., Wu, W.W., Li, Q.Z., Li, K.T., 2018a. Structural and magnetic properties of soft/hard NiFe2O4@SrCo0.2Fe11.8O19 core/shell composite prepared by the ball-milling-assisted ceramic process. J. Mater. Sci. Mater. Electron. 29, 13903–13913.

Xia, J.Y., Shen, Y.L., Xiao, C.Y., Chen, W., Wu, X.H., Wu, W.W., Wang, Q.S., Li, J.T., 2018b. Structural and magnetic properties of soft/hard Mn0.6Zn0.4Fe2O4@Sr0.85Ba0.15Fe12O19 core/shell composite synthesized by the ball-milling-assisted ceramic process. J. Electron. Mater. 47, 6811–6820.

Xiong, R., Li, W., Fei, C., Liu, Y., Shi, J., 2016. Exchange-spring behavior in BaFe12O19-Ni0.5Zn0.5Fe2O4 nanocomposites synthesized by a combustion method. Ceram. Int. 42, 11913–11917.

Yue, Z., Guo, W., Zhou, J., Gui, Z., Li, L., 2004. Synthesis of nanocrystilline ferrites by sol–gel combustion process: the influence of pH value of solution. J. Magn. Magn. Mat. 270, 216–223.

Yang, H., Ye, T., Lin, Y., Liu, M., Kang, P., Zhang, G., 2016. Enhancements of (BH)max and remanence in BaFe12O19/CaFe2O4/CoFe2O4 nanocomposite powders by exchange-coupling mechanism. Mater. Chem. Phys. 171, 27–32.

Yang, H., Liu, M., Lin, Y., Yang, Y., 2015. Simultaneous enhancements of remanence and (BH)max in BaFe12O19/CoFe2O4 nanocomposite powders. J. Alloys Compd. 631, 335–339.

Zhang, Z., Liu, X., Wang, X., Wu, Y., Li, R., 2012. Effect of Nd-Co substitution on magnetic and microvawe adsorbtion properties of SrFe12O19. J. Alloy Compd. 525, 114–119.